Journal of Materials Chemistry A

ROYAL SOCIETY OF CHEMISTRY

PAPER

View Article Online
View Journal | View Issue

Cite this: J. Mater. Chem. A, 2022, 10, 10557

One-step fabrication of robust lithium ion battery separators by polymerization-induced phase separation†

Alexander J. Manly[a] and Wyatt E. Tenhaeff *[ab]

Conventional lithium ion battery separators are microporous polyolefin membranes that play a passive role in the electrochemical cell. Next generation separators should offer significant performance enhancements, while being fabricated through facile, low cost approaches with the ability to readily tune physicochemical properties. This study presents a single-step manufacturing technique based on UV-initiated polymerization-induced phase separation (PIPS), wherein microporous separators are fabricated from multifunctional monomers and ethylene carbonate (EC), which functions as both the pore-forming agent (porogen) and electrolyte component in the electrochemical cell. By controlling the ratio of the 1,4-butanediol diacrylate (BDDA) monomer to ethylene carbonate, monolithic microporous membranes are readily prepared with 25 μm thickness and pore sizes and porosities ranging from 6.8 to 22 nm and 15.4% to 38.5%, respectively. With 38.5% apparent porosity and an average pore size of 22 nm, the poly(1,4-butanediol diacrylate) (pBDDA) separator takes up 127% liquid electrolyte, resulting in an ionic conductivity of 1.98 mS cm^{-1}, which is greater than in conventional Celgard 2500. Lithium ion battery half cells consisting of $LiNi_{0.5}Mn_{0.3}Co_{0.2}O_2$ cathodes and pBDDA separators were shown to undergo reversible charge/discharge cycling with an average discharge capacity of 142 mA h g^{-1} and a capacity retention of 98.4% over 100 cycles – comparable to cells using state-of-the-art separators. Moreover, similar discharge capacities were achieved in rate performance tests due to the high ionic conductivity and electrolyte uptake of the film. The pBDDA separators were shown to be thermally stable to 374 °C, lack low temperature thermal transitions that can compromise cell safety, and exhibit no thermal shrinkage up to 150 °C.

Received 16th December 2021
Accepted 7th April 2022

DOI: 10.1039/d1ta10730e

rsc.li/materials-a

Introduction

Lithium ion batteries (LIB) provide reversible electrochemical energy storage by shuttling lithium ions between two intercalation-type electrodes. The medium for ion transport is aprotic organic electrolyte, and thin polymeric separators physically separate the electrodes. Advances in LIB technology are necessary to meet society's goals of further electrifying transportation and decarbonizing the electrical grid.[1–3] Throughout the history of LIB development, significant research and development effort has focused on advancing the cathode, anode, and electrolyte.[4] While the separator is often considered a passive cell component, it too plays a critical role in determining the cost, reversibility, power density, and overall safety of LIB cells.[5]

State-of-the-art separators in commercial LIBs are microporous polyolefin membranes with thicknesses ≤25 μm.[6] Fabricated from high-volume, commodity polyolefin feedstock, these separators are favored due to their low cost, chemical inertness, low density (limiting mass added to the cell), and sufficient mechanical properties.[7] However, these separators account for roughly 15% of the material cost of commercial LIBs, making them the second most expensive component in LIB cells.[8] For this reason, there is research underway to develop multifunctional separators, which can contribute to the chemical and physical stability of LIBs, rather than being purely passive.[9–11] The surface energy of polyolefin separators is also non-ideal; the purely aliphatic, non-polar surface leads to poor wettability by highly polar electrolytes, limiting electrolyte uptake and ionic conductivity.[12] Furthermore, polyolefin separators have insufficient safety features in high-voltage applications such as electric vehicles and stationary storage, due to thermal shrinkage and melting at modest temperatures.[13–15] These factors motivate research for new polymeric materials for LIB separators.

When developing separators, it is necessary to carefully consider the fabrication process to achieve the desired polymer chemistry and physicochemical properties. Commercial polyolefin separators are fabricated by both wet and dry processes.[6] In efforts to improve upon polyolefin separators, a myriad of

[a]Materials Science Program, University of Rochester, Rochester, New York 14627, USA
[b]Department of Chemical Engineering, University of Rochester, Rochester, New York 14627, USA. E-mail: wyatt.tenhaeff@rochester.edu

† Electronic supplementary information (ESI) available. See DOI: 10.1039/d1ta10730e

other polymer chemistries have been explored, prepared through a diverse set of fabrication procedures. These methods have been reviewed in-depth over the last ten years.[6,12,16,17] At the laboratory scale, the vast majority of microporous separators are fabricated from polymer solutions using pre-synthesized polymers and some method of phase inversion, including thermally-induced phase separation (TIPS),[18,19] evaporation-induced phase separation,[20,21] non-solvent induced phase separation (NIPS),[22–31] and other mechanisms.[32–36] These methods are similar in that they require multiple processing steps, such as solution casting of a film followed by solvent extraction, which are both energy-intensive and time-consuming. The solvent must be thoroughly removed as it is often chemically unstable in the LIB cell. Furthermore, the solvent system and fabrication method must be tailored specifically to the chemistry and properties of the polymer, which serves as a roadblock for the modulation of separator properties.

In the polymerization-induced phase separation (PIPS) process, monomer and porogen precursors are chosen such that they are miscible and initially form a homogeneous solution. UV photopolymerization of the solution leads to polymer chain growth and network formation (if using multifunctional monomers), which reduces the polymer solubility and leads to spinodal decomposition of the solution into two continuous phases.[37] At a sufficient molecular weight, network formation arrests the long-range diffusion of polymer chains, effectively freezing the separated phases and resulting in a monolithic polymer phase with a porous morphology.[38] PIPS has deep roots in other areas of research, such as the fabrication of ion-exchange membranes and chromatography.[39,40] However, it has only been employed a handful of times in the LIB literature. PIPS has been employed with epoxy chemistry to create microporous films for LIB applications.[41,42] These studies show that reasonable ionic conductivities can be obtained, but often at the expense of mechanical properties. Furthermore, while the porous monoliths in both studies were designed for use in LIBs, their performance in LIB cells was not reported. PIPS has also been used in several attempts to create a structural solid battery electrolyte, wherein a mechanically strong polymer is chosen to provide strength, while the pore volume contains ionic liquids or polymer-ionic liquid mixtures to provide ion transport.[43–45] PIPS has been used to fabricate composite structural battery electrodes with aprotic liquid electrolytes. In these studies, carbon fiber electrodes are infused by PIPS precursor solutions which are then reacted by UV-initiated or thermally-initiated polymerizations.[46,47] This results in a load-bearing polymer phase, and an ionically conductive liquid phase for ion transport. However, these systems still require a separator film between the negative electrode composites and other electrode.

In this study, we report the fabrication of microporous LIB separators using PIPS, outlined in Fig. 1. The novelty of this approach stems from the use of ethylene carbonate (EC) as the porogen. EC is an effective porogen in PIPS, rapidly undergoing phase separation due to its high dielectric constant and poor solvating power for polymers. It is also crystalline at room temperature, which leads to a reduction in phase separated

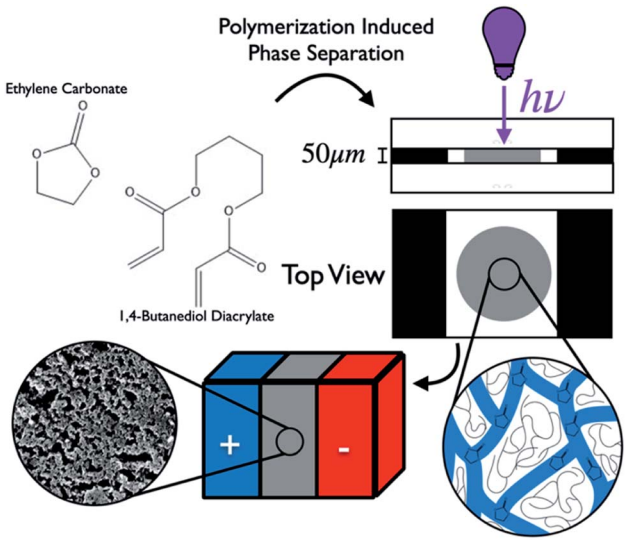

Fig. 1 Outline of the fabrication of a porous monolith using monomer 1,4-butanediol diacrylate (BDDA) and porogen ethylene carbonate (EC). UV polymerization induces a microphase separation and results in a porous film that is incorporated into an electrochemical cell.

dimensions. But EC is also an indispensable component of state-of-the-art LIB electrolytes. Thus, using this approach, EC does not need to be extracted from the film, significantly simplifying the fabrication process. Furthermore, this PIPS system eliminates the use of solvents during fabrication, in constrast to more traditional laboratory methods. In essence, this process presents a pathway to one-step manufacturing of separators. We first explore the structure and properties of microporous separators prepared using the multifunctional monomer, 1,4-butanediol diacrylate (BDDA), and EC. For this study, the EC is extracted through a solvent washing step to reveal the porous morphology of the separators. After thoroughly characterizing these membranes, EC-in-polymer separators were fabricated, where no post-processing is performed, and the film is instead assembled directly into lithium ion battery half cells for electrochemical performance characterization. Throughout the study, the commercial polypropylene (PP) separator Celgard 2500 is used as a benchmark. These PIPS separators compete favorably with PP separators, and offer a platform for further materials development through the tunability of polymer composition and properties through photopolymerization.

Experimental

Materials and separator fabrication

All chemical reagents and components were used as-received from the manufacturer, and stored as recommended. Technical grade 1,4-butanediol diacrylate (BDDA), ≥87% purity, and anhydrous ethylene carbonate (EC), 99% purity, were purchased from Sigma-Aldrich. 2-Benzyl-2-(dimethylamino)-4′-morpholino butyrophenone (Omnirad 369) was a gift from IGM Resins. Standard conductivity solutions made of aqueous KCl were

purchased from Fisher Scientific. $LiNi_{0.5}Mn_{0.3}Co_{0.2}$ (NMC532) positive electrodes used in this experiment were produced at the U.S. Department of Energy's (DOE) CAMP (Cell Analysis, Modeling and Prototyping) Facility, Argonne National Laboratory. The cathode material was 90 wt% NMC532, 5 wt% Timcal C45 (conductive additive), and 5% Solvay 5130 PVDF binder. The coating thickness was 34 μm and the areal loading density 9.12 mg cm^{-2}. The battery electrolyte was 1 M $LiPF_6$ in 3 : 7 v/v ethylene carbonate/dimethyl carbonate, purchased from MTI Corporation. Celgard 2500 was a gift from Celgard.

PIPS precursor solutions were first prepared by mixing the appropriate amount of BDDA and EC in a scintillation vial, with 0.1 wt% of Omnirad 369 initiator. Samples are labelled as (p) BDDA*XX*, where *XX* is the mass percent of EC incorporated. This mixture was capped and sonicated for 20 minutes until a homogeneous solution is obtained. Three drops of the precursor solution were placed on a 2″ × 3″ glass slide. A second glass slide was set on top of the solution to spread it out. This method resulted in films of 20–25 μm in thickness. Thicker films were obtained using 50 μm-thick pressure adhesive tape as spacers. The slides were then placed under a long-wave UV lamp (20 mW cm^{-2}) for 10 minutes, flipping the slides halfway through the cure.

After the cure, the slides were carefully separated using a razor blade. If removal of the porogen was required, the solid polymer film was placed in an acetone bath. The films were rinsed with fresh acetone three times to remove any residual EC, and dried on a clean aluminum pan at 70 °C overnight. The films could then be cut or punched into whatever size or shape was necessary, and their thickness verified using a Pittsburgh digital micrometer.

Compositional and physical characterization

Fourier transform infrared spectroscopy (FTIR). IR absorption spectra were obtained throughout the fabrication of the porous polymer: precursors before polymerization, after UV-initiated PIPS, and after washing and drying. Spectra were obtained on a Nicolet iS50 FT-IR using a single reflection Specac Golden Gate attenuated total reflectance (ATR) attachment. Sixty-four spectra were integrated at a resolution of 4 cm^{-1}.

Electrolyte uptake. The mass of dry separators ($m_{separator}$) was first measured. They were then soaked in battery electrolyte. The wet samples were dabbed so excess electrolyte on the surface of the sample was removed. Once the mass of the soaked sample was equilibrated, it was recorded. The difference between this wet mass and the dry separator mass was the mass of electrolyte taken up by the separator ($m_{electrolyte}$). The electrolyte uptake could then be computed by:

$$\%\ \text{Uptake} = \frac{m_{electrolyte}}{m_{separator}} \quad (1)$$

This measurement was repeated with four separate samples for each material, and the results were averaged to reduce experimental error.

Thermogravimetric analysis (TGA). Thermal stability of samples was tested on a TA Instruments Discovery TGA under a nitrogen purge flow of 25 mL min^{-1}, from 50–700 °C with a ramp rate of 5°C min^{-1}.

Differential scanning calorimetry (DSC). DSC was performed on a TA Instruments DSC Q2000, using TZero aluminum pans and hermetic lids. Under a nitrogen purge of 50 mL min^{-1}, samples were ramped at 10 °C min^{-1} from 0 °C to 200 °C four times to ensure repeatability.

Thermal shrinkage. Separators were prepared using above methods, and punched into a circular shape. Celgard 2500 samples were also punched into a circular shape. A digital image of each separator material was taken in front of a piece of paper with a known 5″ × 5″ area at room temperature, after heating to 90 °C for 30 minutes, and after heating to 125 °C for 30 minutes. Computer vision analysis was used to compute the area of the separator materials for each image, enabling the quantitative comparison of separator areas before and after heating. This procedure was performed in triplicate to ensure consistent results.

Scanning electron microscopy (SEM). Observations were made using a Zeiss Auriga SEM/FIB at an accelerating voltage of 3 kV. Prior to observation, all EC was removed from the samples as described above, which were then sputter coated with gold on a Denton Vacuum DESK-II DC sputtering system. Samples were sputter coated for 60 seconds, leading to a coating of about 70 Å. From the SEM micrographs, porosity estimates were obtained with a computer vision algorithm which detects the fraction of area occupied by pores in the sample image, using brightness thresholding and contour detection methods from the openCV Python library.[48] SEM images with the detected contours overlaid are reported in Fig. S1.†

Mechanical testing. Stress–strain curves were obtained using a TA Instruments RSA-G2 solids analyzer. Samples were cut to a 6 × 12 mm rectangle, and their thickness was measured using a digital micrometer in order to know the cross-sectional area of the sample. Samples were clamped on each end with an initial gap of 5 mm. Samples were equilibrated to 25 °C, and a strain sweep was performed at a strain rate of 0.67%/s.

Contact angle measurements. Static water contact angles (WCAs) were obtained using a Biolin Scientific Theta Lite Tensiometer. Samples were laid flat on the bed, and a digital video was recorded as a single drop of was dispensed on the surface. A frame was chosen after the contact angle equilibrated.

Electrochemical characterization

Electrochemical impedance spectroscopy (EIS). The ionic conductivities were determined using AC impedance spectroscopy. Polymer films were tested using a Swagelok T-cell, where the film is held between two blocking stainless steel electrodes with a diameter of 3/8″. The inner cavity was then filled with battery electrolyte, ensuring full uptake, and the openings were tightly capped. These T-cells were constructed inside an argon-filled glovebox, but then removed for testing. The cells were placed inside a Tenney Jr environmental chamber, and connected to a Solartron SI 1260 impedance analyzer using a two-electrode setup. Before each measurement, the cell was

equilibrated to the desired temperature for 45 minutes. Sweeps were performed from a frequency of 1 MHz to 0.1 Hz, with an AC amplitude of 10 mV. The ionic resistances were simply taken to be the real impedance intercept on the resulting Nyquist plot. In order to account for ohmic and contact resistances introduced by the Swagelok T-cells, and increase confidence in reported ionic conductivities, measurements were performed on three different thicknesses for each material. For Celgard 2500, membranes were layered to vary the thickness. The resistivity of each sample was then obtained by taking the slope of resistance*area *vs.* thickness.

The ionic conductivity of the battery electrolyte was measured using an Accumet 2-cell conductivity probe connected to the same Solartron impedance analyzer inside an environmental chamber. This probe was first calibrated using a series of standard KCl solutions (447 μS cm^{-1}, 1000 μS cm^{-1}, 8974 μS cm^{-1} and 15 000 μS cm^{-1}).

Arrhenius plots were obtained by performing the above measurements and analyses at 0 °C, 10 °C, 20 °C, 25 °C, 30 °C, 40 °C, and 50 °C.

Construction of electrochemical half cells

In order to test the separators, electrochemical half-cells were constructed using a CR2032 coin cell format, entirely in an argon-filled glovebox. The half-cell format was used to eliminate as many variables as possible. The negative electrode was fabricated by first cutting off a piece of lithium ribbon, and scraping off the oxide layer with a wire brush. The lithium was then rolled flat with a piece of PVC tubing, and punched to a diameter of 5/8″ using a hollow punch. These operations were performed on top of a clean polypropylene sheet.

A piece of positive electrode material was cut off using scissors, placed inside a folded piece of weighing paper, and electrodes were punched out to a diameter of 1/2″ using a paper punch.

The cell was constructed in the following order: the negative electrode cap was placed down, a wave spring placed inside, and a stainless-steel spacer placed on top of that. The lithium electrode was then centered on this spacer. Battery electrolyte was dropped onto the lithium, and the separator was placed on this electrolyte to allow wetting. Electrolyte was dropped on the positive electrode to allow wetting of the porous active material, and then set on top of the separator, being sure to center the positive electrode with the lithium, to ensure full overlap. The positive electrode cap was then pressed onto the negative electrode cap, and the full construction was crimped in a MTI MSK-160D electric crimper. The coin cells were then removed from the glovebox, wiped down with acetone, and labelled.

Electrochemical cycling

Cells were cycled at 30 °C using a Neware battery testing system. Cycling procedures were adapted from Argonne National Lab's published protocols for testing LIBs.[49] The first step of all cycling was a formation step. This consisted of first applying a tap charge of 1.5 V for 15 minutes. The cells were then rested for 6 hours to allow for full electrolyte wetting and equilibration. The cells were then cycled twice at a C/10 rate.

The long-term performance of cells was tested by cycling the cells at C/3 for 100 cycles between 3 V and 4.2 V. The charging steps used a C/20 cut-off current while the discharge steps simply cut-off at 3 V.

A rate performance test was performed by cycling at several current densities. After formation, cells were discharged to 3 V for 5 cycles at the following rates: C/5, C/2, 1C, 2C, 3C and C/5 again. After each discharge, the cells were charged to 4.2 V with a C/5 cut-off current. Five cells were successfully cycled 100 times for each material.

Results and discussion

In the idealized PIPS process, an initially homogenous solution of monomer and porogen is made to phase separate through spinodal decomposition as the monomer is converted to polymer reducing its miscibility with the porogen.[37,38] As this separator fabrication concept utilizes EC as both the porogen and electrolyte component in the assembled electrochemical cell, it is critical that EC does not participate in the polymerizations reactions that would immobilize it and/or alter its properties. FTIR spectra of the precursor solutions and polymeric materials in the PIPS process are provided in Fig. 2a. The spectra were normalized to the intensity of the carbonyl stretching mode of the acrylate group around 1720–1730 cm^{-1} to observe relative changes in other chemical functionalities and components. The C=C stretch modes of BDDA at 1615 cm^{-1} and 1645 cm^{-1} that are present in the precursor solution (BDDA/EC) essentially disappear completely after photopolymerization, while the other peaks in the fingerprint region of the spectra remain at the same wavenumber suggesting that only conversion of the acrylate double bonds has occurred. A small peak at 1450 cm^{-1} emerges during polymerization and remains after the removal of porogen. This peak corresponds to the bending mode of the CH_2 groups on the newly formed aliphatic polymer backbone.[50] The fractional conversion of the double bonds was not quantified, but the resulting solid membrane becomes mechanically robust and insoluble in organic solvents, which is indicative of network formation. Fig. 2b shows that before and after polymerization, the high intensity stretch modes of the C=O carbonyl bonds in EC are unchanged. These peaks at 1775 cm^{-1} and 1805 cm^{-1} are split by Fermi resonance resulting from the short-range ordering of the strong carbonyl dipoles.[51–53] Throughout the polymer synthesis these characteristic peaks remain unchanged, indicating that EC is inert and non-reactive throughout the PIPS process. If EC were to undergo a ring-opening polymerization reaction, the carbonyl stretch peaks would be expected to consolidate into a single peak at 1740 cm^{-1}, which is not observed.[54] We also observed the complete disappearance of the EC carbonyl stretching peaks after the acetone washing of the polymer, indicating that EC was not incorporated or immobilized in the polymer chemical structure. Therefore, EC is a suitable porogen for PIPS.

An important feature of the PIPS process is the ability to readily tune the membrane structure through the precursor

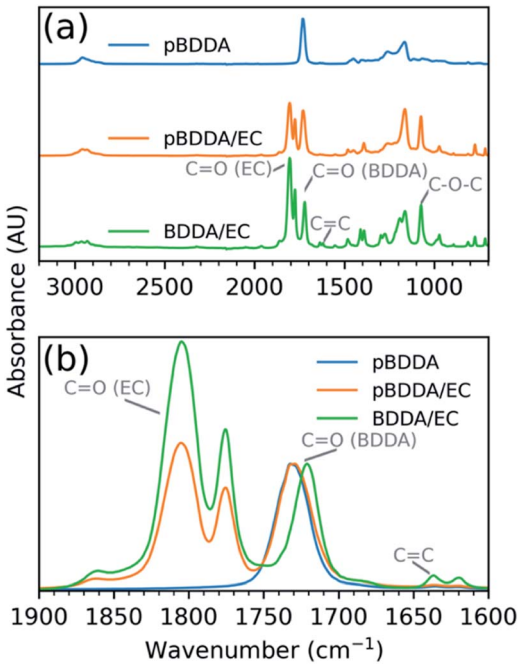

Fig. 2 FTIR-ATR spectra normalized to the monomer carbonyl peak at 1720 cm^{-1} showing (a) offset full spectra and (b) overlaid spectra in a key range illustrating the polymerization of BDDA and subsequent removal of EC. BDDA/EC is the precursor mixture, pBDDA/EC is the film after polymerization, prior to EC extraction with acetone, and pBDDA is the remaining polymer after EC extraction.

composition. The effect of the porogen concentration on membrane properties is clearly indicated through the digital photographs shown in Fig. 3a. Low EC concentrations resulted in lower porosity and smaller pore sizes, and the membrane is translucent. As the EC concentration increases in the polymerization solution, both the porosity and pore sizes increased, resulting in more scattering of light. Hence, the membranes become increasingly opaque. Image analysis of scanning electron micrographs in Fig. 3b–e was used to quantify percent apparent porosity and pore sizes in the membranes. The results are listed in Table 1, with a maximum average pore radius of 22 nm and the apparent porosity of 38.5% obtained with the 60 wt% EC composition. For context, these values are typical of commercial LIB separators, which can have porosities ranging from 34% to 85%, and average pore radii ranging from 13.5 nm to 32 nm.[5,55] The histogram plots in Fig. S2† show the distribution of pore radii. It was found that small pores dominate the collection of pores in all formulations, with slight shifting towards larger radii in the more-porous separators. Generally, LIB separators must have a pore size of <1 μm in diameter to prevent small particles of active material from passing through the membrane.[56] However, much smaller pores are advantageous because they enable the LIB to operate at higher currents while still suppressing lithium dendritic growth on graphite anodes by eliminating excess ion diffusion gradients.[57] Thus, the length scale of the pores in pBDDA60 is ideal for LIB applications.

To assess the surface energy of the membrane, which is critical for compatibility with high polarity electrolyte solutions, static water contact angles (WCAs) were measured and provided in Fig. 3f–i. Despite the invariant polymer composition, the WCA decreased from 57.8° (pBDDA30) to 33.8° (pBDDA60); this effect is attributed to membrane porosity. During water contact angle experiments, it was observed that pBDDA30 and pBDDA40 did not uptake any water, while pBDDA50 was able to uptake some water, and pBDDA60 even more, which correlates with the membrane porosity. The decrease in contact angle is due to a transition from the Cassie–Baxter state to the Wenzel state as the pore size increases.[58]

pBDDA consistently shows a lower WCA than the commercial Celgard 2500 separator, which was measured as 87.5°. Table 1 shows that the WCA in pBDDA30, which is highest of all the pBDDA samples, is still lower than that of Celgard 2500 (Table 1). Despite the higher apparent porosity in Celgard, the pBDDA surface is more polar, forming stronger, longer-range interactions with polar solvents (and can undergo hydrogen bonding interactions with water). The polypropylene comprising Celgard 2500 is purely aliphatic and does not possess these interactions. The greater polarity of pBDDA films is expected to be advantageous in LIB applications, promoting electrolyte uptake and facilitating Li^+ transport.[59,60] Indeed, it was found that liquid electrolyte was greater in pBDDA60 (127%) than Celgard 2500 (98%). As expected, electrolyte uptake was directly correlated to porosity. This is illustrated by the observation that a 27% increase in apparent porosity from pBDDA50 to pBDDA60 resulted in a 90% increase in electrolyte uptake.

Ion transport is inextricably linked to the electrolyte uptake of the membranes. Electrochemical impedance spectroscopy (EIS) was employed to determine ionic conductivities of the electrolyte-laden separators. Because the Swagelok T-cell design introduces significant contact resistances, three samples of each membrane were prepared at different thicknesses. This allowed the contact resistance to be reliably quantified and provided a more robust measurement of the transport properties over a range of practical membrane thicknesses. The effective ionic conductivity in pBDDA60 at 25 °C was found to be 1.98 ± 0.08 mS cm^{-1}, which is slightly higher than for Celgard 2500 (1.62 ± 0.13 mS cm^{-1}). The greater electrolyte uptake in pBDDA compensated for its lower porosity relative to Celgard. As expected, pBDDA samples formulated with less EC resulted in lower ionic conductivities, below 1 mS cm^{-1}, and thus will be less relevant for high power energy storage cells. The effective ionic conductivities reported for pBDDA separators fall within a range which is typical for non-woven monolayer microporous separators. Separators have been reported with ionic conductivity as low as 0.11 mS cm^{-1}, and as high as 7.8 mS cm^{-1}, though 0.5–3.5 mS cm^{-1} is most typical, but can vary with the electrolyte utilized.[17,56,61] A useful metric for characterizing and comparing LIB separators is

$$N_M = \frac{\sigma_0}{\sigma_{eff}} \quad (2)$$

where σ_0 is the ionic conductivity of the liquid electrolyte, and σ_{eff} is the effective ionic conductivity of the saturated porous

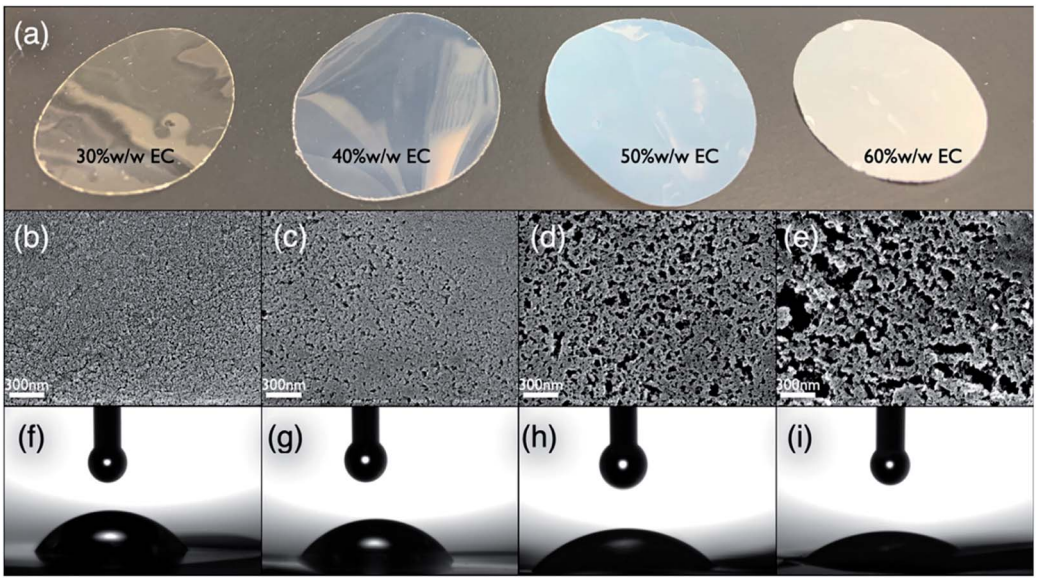

Fig. 3 (a) Digital images of microporous pBDDA separators fabricated with a range of porogen concentrations, after removing porogen (from left to right: pBDDA30, pBDDA40, pBDDA50, and pBDDA60). Corresponding SEM images and static water contact angle experiments of pBDDA films made with (b, f) 30% w/w EC, (c, g) 40% w/w EC, (d, h) 50% w/w EC, and (e, i) 60% w/w EC. All SEM images were taken at 50 000× magnification.

membrane.[55,62] This metric is ideal for LIB separator characterization as it controls for the electrolyte conductivity and correlates to the expected internal resistance expected when incorporated into an electrochemical cell. As N_M approaches unity, the ionic conductivity of the wetted membrane approaches the ionic conductivity of pure electrolyte, and there is negligible added resistance from the membrane. Thus, a lower N_M is preferred in LIB applications to minimize polarization effects at all temperatures. Using eqn (1), N_M was calculated for all porous membranes characterized. For Celgard 2500, N_M was measured as 5.9, while the more-conductive pBDDA60 had a N_M of 4.8. Despite having a lower porosity than Celgard 2500, the pBDDA60 sample exhibited a higher ionic conductivity/lower N_M. This can be explained by surface energies considerations, where the interactions of pBDDA with the battery electrolyte solvent and salt are more favorable than for polypropylene of Celgard.

When compared to commercial separators, pBDDA60 has an exceptional MacMullin number. The N_M of many commercial LIB separators are listed in Table S1.† According to Landesfeind *et al.* the following separators have a N_M greater than pBDDA60: (1) Celgard H2013, 2320, 2325, 3500, and C480, (2) PET membrane Separion S240P30, and (3) two unnamed HDPE membranes.[63] Only non-woven PET membrane Freudenberg FS-3001-30 and Celgard 2500 were reported to have lower MacMullin number than pBDDA60, at 4.6 and 4.5, respectively. This Celgard 2500 measurements is in slight disagreement with our measurements. However, it should be noted that other studies have reported N_M of 8.5, 13 and 18 for Celgard 2500.[55,62,64] Djian *et al.* also report MacMullin numbers >4.8 for commercial separators Celgard 2400, 2730, and Solupor 14P01A, 3P07A and 10P05A, while Patel, *et al.* report N_M > 16 for Hipore N962C, N720, and 6022.[62,64] A general requirement for battery separators is to have a MacMullin number of <8, which is far exceeded by pBDDA60.[7]

Fig. 4 presents the ionic conductivity of the liquid electrolyte as a pure solution and within the microporous separators. Confidence in these data points is illustrated by the shaded area behind them. The confidence intervals for less-conductive separators appear larger in Fig. 4 due to the logarithmic scale

Table 1 Physical properties of pBDDA films fabricated with varying amounts of porogen and commercial polypropylene separator Celgard 2500

Sample	Porosity (%)	Average pore radius (nm)	Electrolyte uptake (%)	Conductivity @25 °C (mS cm^{-1})	MacMullin number	Activation energy (kJ mol^{-1})	Contact angle (°)	Modulus (MPa)
pBDDA30	15.4	6.8	45	0.27 ± 0.06	35.2	16.2 ± 3.5	57.3	480
pBDDA40	17.0	9.1	50	0.26 ± 0.02	36.4	18.5 ± 3.5	56.8	429
pBDDA50	30.4	17.2	67	0.93 ± 0.06	10.2	16.5 ± 1.0	48.3	357
pBDDA60	38.5	22.0	127	1.98 ± 0.08	4.8	13.4 ± 1.6	33.8	246
Celgard 2500	55.0[a]	32.0[a]	98	1.62 ± 0.13	5.9	13.4 ± 1.1	87.5	729(MD), 273(TD)

[a] Values reported by manufacturer.

of the *y*-axis. The absolute confidence intervals reported in Table 1 indicate that the error in conductivity measurements is consistent between the separators. The temperature dependence of ionic conductivity is similar among all of the separators and can be described by the Arrhenius relationship, which is a manifestation of the temperature dependence of the solvated ion diffusivities over this limited temperature range.[65] Activation energies of ionic conductivity were determined through linear regression of ln σ_{eff} *vs.* T^{-1} and are tabulated in Table 1. The activation energy of the liquid electrolyte was found to be 13.8 ± 0.3 kJ mol^{-1}. Nearly identical activation energies of 13.4 + 1.1 kJ mol^{-1} and 13.4 ± 1.6 kJ mol^{-1} were found for the Celgard 2500 and pBDDA60 samples, respectively. This implies that (1) the mechanism for ionic conductivity is diffusion through the liquid electrolyte phase within the porosity of the microporous separators and (2) significant additional energetic barriers to electrolyte diffusion are not introduced by the separators. This is expected given the porous morphology characterized by SEM and is consistent with numerous previous studies. There appears to be a slight increase in activation energy in the less porous pBDDA membranes. This is likely explained by these membranes containing a small fraction of closed porosity, which requires another mechanism of transport, potentially through a gel phase between polymer chains.

The electrochemical performance of pBDDA membranes was assessed in NMC532/Li half cells and compared to the Celgard 2500 benchmark in Fig. 5 and 6 pBDDA60 was selected for this characterization as it has the highest apparent porosity and conductivity among all the separators. The charge/discharge capacities and coulombic efficiencies over 100 cycles is provided in Fig. 5. While cycling between 3.0 to 4.2 V, an average discharge capacity of 142 mA h g^{-1} was achieved with 98.4% capacity retention over the 100 cycles. Given the similar ion transport properties and separator thicknesses of pBDDA60 and Celgard 2500, the near identical cycling performance with the two separator materials is expected. The stability over 100 cycles is strong evidence for the compatibility of pBDDA in modern LIB cells. The individual charge/discharge voltage profiles at cycles 1, 50 and 100 provide further evidence of the electrochemical stability. The voltage profiles in Fig. 5b–d are essentially identical for the two separators and show the sloping discharge to approximately 3.6 V with little voltage hysteresis, which is typical of NMC532.[66] Additional voltage excursions and/or capacity irreversibility signifying chemical instability or other side reactions are not observed. The coulombic efficiencies (CEs) on the order of 99% are typical for half-cell formats, where parasitic reactions on the Li metal may lead to lower CE than graphite anodes.[67,68] Five cells were prepared and cycled using each separator material to improve statistical confidence in his comparison; the average discharge capacity and CE are plotted with the standard deviation in Fig. S3.† This data highlights that the observed cycling performance was highly reproducible over many attempts.

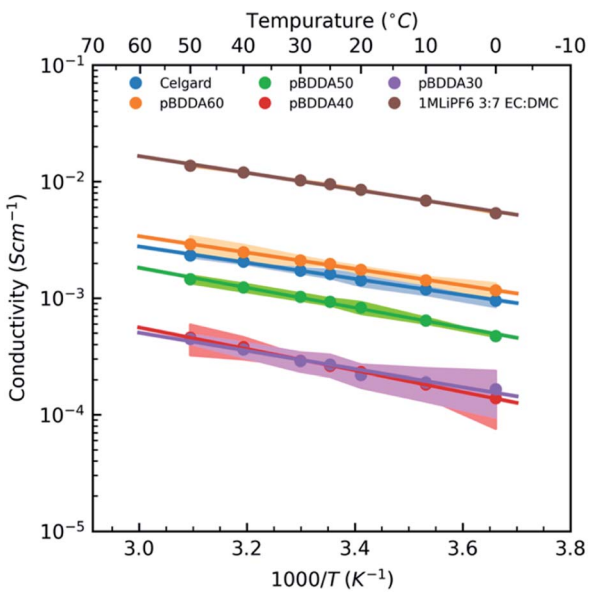

Fig. 4 Conductivity of Celgard 2500 and pBDDA samples as a function of temperature. Effective conductivity measurements were performed used 1 M $LiPF_6$ in 3 : 7 v/v EC/DMC. Confidence in conductivity measurements are illustrated as shaded backgrounds behind the data.

To understand the impact of the pBDDA separator properties on the power performance of LIB cells, a rate test with incremented discharge currents was performed (Fig. 6). With Celgard 2500 separators, increasing the discharge current from C/10 to 3C resulted in a capacity drop from 143.5 to 121.0 mA h g^{-1}, or 15.7%. Using pBDDA, the cell exhibited a higher capacity which can be attributed to the separator having higher effective ionic conductivity, which reduces the area specific resistance, as well as random variations in electrode loading. At C/10, a discharge capacity of 151.3 mA h g^{-1} is achieved, which decreases to 123.9 mA h g^{-1} at 3C (18.1% drop). With both separators, the low rate (C/5) capacity recovers after the rate testing, suggesting that separators provide for efficient ion transport and undesirable side reactions at high rates are not observed. This is again illustrated by the voltage profiles in Fig. 6b–g. The expected voltage profiles for NMC532 are obtained. The primary difference between Celgard 2500 and pBDDA60 cells is that additional cathode utilization occurs with pBDDA, which can be attributed to the lower concentration polarization since it is slightly more conductive than Celgard. The voltage curve "knee" is delayed in the pBDDA cells suggesting a lower internal impedance and therefore voltage loss, allowing for a greater depth of discharge as the lithiated active material is depleted.[5] CE dropped temporarily with each current increment due to increased polarization preventing the cell from experiencing the same depth of discharge as the previous rate. The CE then recovered on subsequent cycles. A CE of >100% was experienced when returning to C/5, as lithium ion reserve in the cathode were recovered due to a decreased polarization at the lower current density. During this return to a lower current density, the discharge capacities of both cells recovered fully.

It was finally demonstrated that PIPS can be used as a single-step, solventless process to fabricate LIB separators. A coin cell was constructed using the same protocols as above,

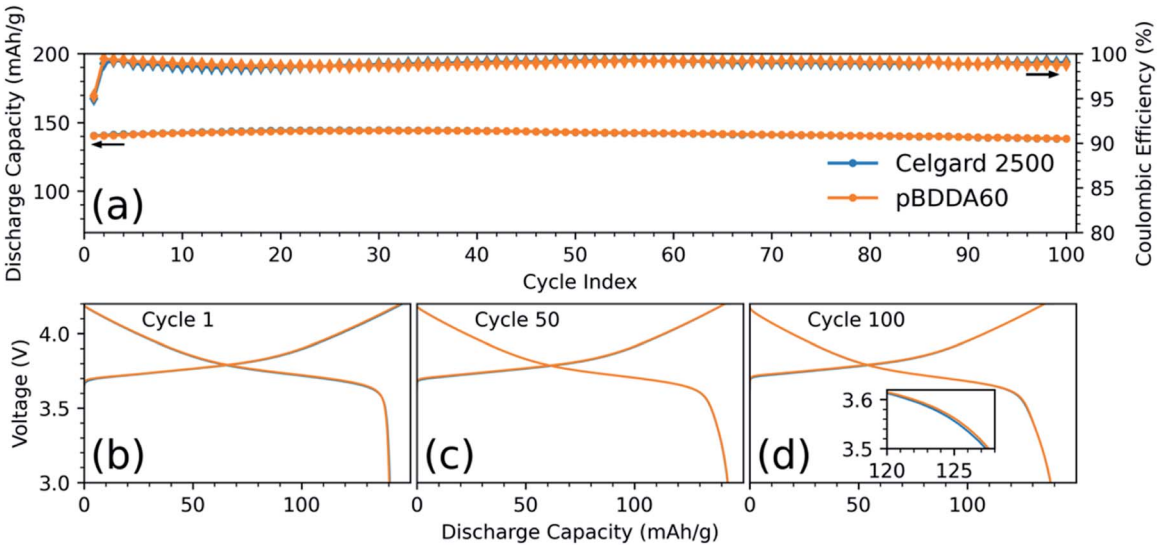

Fig. 5 NMC532/lithium half-cells cycled at C/3. pBDDA60 separator was 28 μm in thickness, and Celgard 2500 is 25 μm in thickness. 1 M $LiPF_6$ in 3 : 7 EC : DMC used as electrolyte. Cycling done at 30 °C. (a) Discharge capacity (circles) and coulombic efficiency (diamonds)are plotted over 100 cycles at C/3 rates after two formation cycles at C/10. Voltage *vs.* discharge capacity profiles are plotted for the (b) 1st, (c) 50th and (d) 100th cycle; inset shows the knee region of the curve to show that performance with both separators is nearly identical.

but polymer films were incorporated into the electrochemical cells immediately after polymerization. No purification or extraction steps were performed – the EC remained in the film. The battery electrolyte was dispensed onto the electrodes and allowed to wet the separator when assembled. This dissolves the EC remaining within the as-prepared separator, yielding a microporous polymer membrane soaked in the $LiPF_6$/EC/DMC battery electrolyte.

The coin cell was cycled using the same aging protocol as the data in Fig. 5. Fig. 7a shows that this electrochemical cell cycles reversibly over 100 cycles. After 100 cycles, the cell started and ended with a capacity of 131.6 mA h g^{-1}. This was accompanied by a slight rise and fall in capacity caused by the wetting of the cathode, and subsequent capacity degradation, which was also observed in cells incorporating the washed separators in Fig. 5 and 6. The lower average capacity (134.2 mA h g^{-1}) when

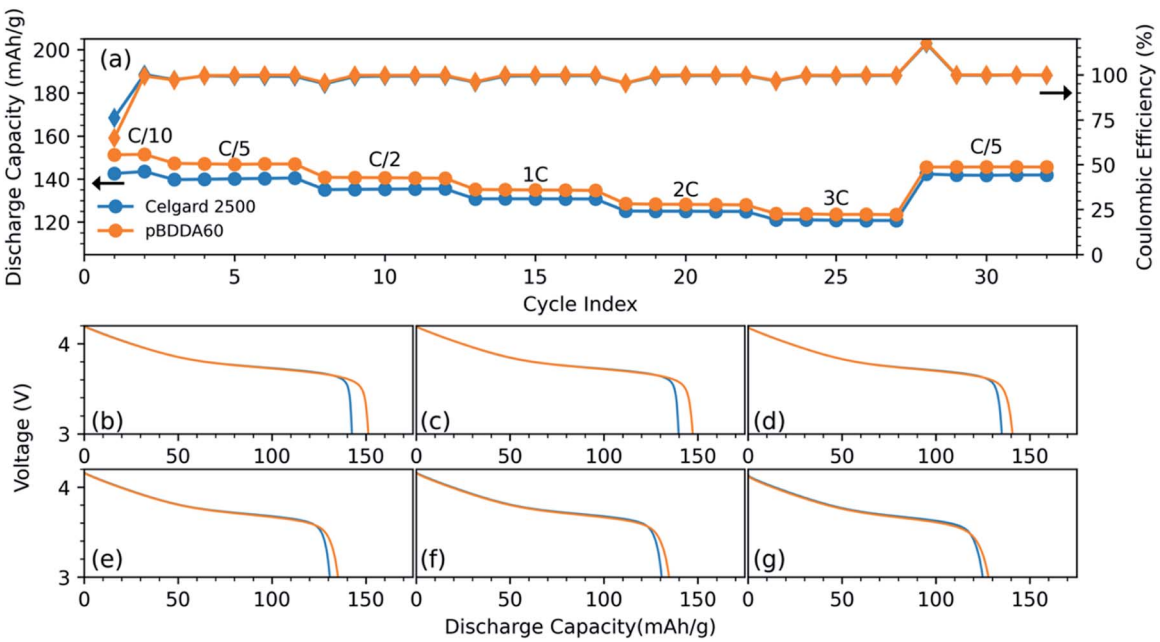

Fig. 6 Results of rate test on NMC532/Li half-cells incorporating Celgard 2500 and pBDDA60 separators. The pBDDA separator was 25 μm in thickness (a) discharge capacities and coulombic efficiencies for all 32 cycles, including the formation step. Voltage curves for discharge of both cells are shown for the first cycle of each rate; (b) C/10, (c) C/5, (d) C/2, (e) 1C, (f) 2C and (g) 3C.

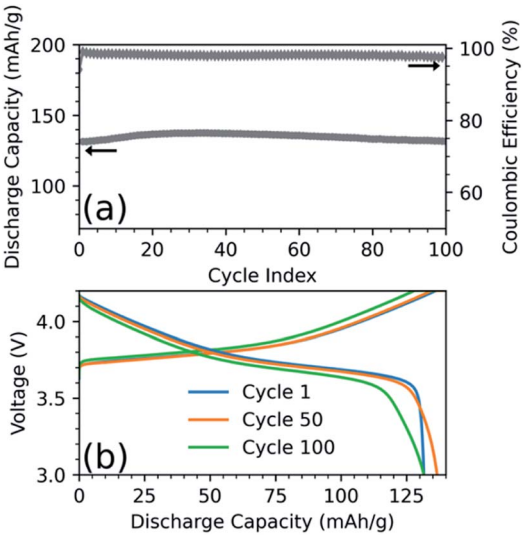

Fig. 7 NMC532/lithium half-cell with 1 M $LiPF_6$ in 3 : 7 v/v EC : DMC, cycled at C/3 at 30 °C. pBDDA60 separator was 50 μm in thickness and incorporated into LIB half-cell without removal of ethylene carbonate to demonstrates single-step manufacturing capability. (a) Discharge capacity (circles) and coulombic efficiency (diamonds) are shown for 100 cycles, and (b) voltage-discharge capacity curves are shown for cycles 1, 50 and 100.

compared to the cells in Fig. 5 and 6 is attributed to the greater thickness of the unwashed film. For ease of handling in a glove box, where the thick gloves limit hand dexterity, this film was fabricated at 50 μm, which introduces a greater ionic resistance when cycling compared to that of the 28 μm pBDDA60 film cycled previously. Fig. 7b shows the voltage-capacity curves of the cell at cycles 1, 50, and 100. Increasing overpotential as the cell is cycled is clearly observed in the space between each curve. This is typical battery degradation caused by the build-up of SEI, increasing the internal cell impedance. These results underscore the ability of this PIPS-based process to eliminate the need for any solvent in fabrication and processing by incorporating EC as porogen during polymer synthesis.

TGA was used to characterize thermal stability of the solvent-washed porous separators in order to avoid contributions from EC. Fig. 8a shows that the onset temperature for decomposition of BDDA is 374 °C compared to 375 °C for Celgard 2500. Around 5% mass of the pBDDA sample remains beyond 500 °C, which can likely be explained by β-scission of the ester functionalities leading to residual carbon char.[69] The thermal stability of both materials is adequate for LIB applications as the alkyl carbonate electrolytes decompose first at 190 °C.[70,71]

Another important thermal consideration is phase transformations at lower temperatures. The differential scanning thermograms in Fig. 8b show that the PP of Celgard 2500 undergoes a first-order melting transition, starting at about 150 °C. pBDDA, on the other hand, lacks thermal transitions up to 200 °C as expected for a highly crosslinked thermoset, suggesting that the separator will maintain its integrity at elevated temperatures. The melting of polyolefins is intended to serve as a safety mechanism to halt thermal runaway. Popular shutdown separators are tri-layer separators consisting of polypropylene and polyethylene (PE) in a PP/PE/PP orientation which act as a thermal fuse around 135 °C when the PE layer melts, filling in the pores, resulting in a large increase in impedance.[15] These types of separators are very useful in low voltage applications such as consumer electronics. However, it has been shown that under high-temperature and high-voltage conditions, such as in electric vehicles and stationary storage, the impedance increase is insufficient, and the relatively low melting temperatures of both PP and PE results in mechanical failure leading to electrode contact and/or decreases in impedance.[13,14] Thus, separators with high thermal stability are desirable in these types of applications. The lack of a melting temperature suggests that pBDDA60 will maintain mechanical integrity under thermal abusive conditions, eliminating the separator as a mode of failure.

A similar safety concern is the thermal shrinkage of polyolefin separators. As a result of internal stresses originating from the uniaxial stretching step in manufacturing of separators such as Celgard 2500, the dimensions of these separators can shrink as the polymer softens at moderate temperatures.[14,15] The shrinking of separators has obvious implications such as allowing contact between battery electrodes. Once again, this failure mode is of greater concern in high power, high-voltage applications where a large amount of heat is generated and non-uniform heating is common.[72,73] Thus, research is underway to develop thermomechanically-stable separator materials.[74] Shown in Fig. 8c, it was found that PP separators begin to shrink long before melting temperatures of PP or PE. A 1.8% area reduction was measured after 30 minutes held at 90 °C, 10.7% after 30 minutes at 125 °C and finally a reduction of 32.8% after 30 minutes at 150 °C. The shrinkage of these PP separators was anisotropic, due to the anisotropic porous structure originating from the uniaxial stretch step during manufacturing. The shrinkage occurred along the machined direction (MD) axis. pBDDA60 exhibited no significant shrinkage at any temperature, underscoring the thermal and mechanical stability of pBDDA60. The thermal stability of pBDDA60 suggests this chemistry and process may be a good candidate for high-power battery applications. Furthermore, if a shutdown feature is desired in a given application, the casting process for fabrication of pBDDA60 can be easily adapted towards coating a layer on top of a polyolefin film, or some other material, to make a bi-layer or tri-layer shutdown separator with superior thermo-mechanical stability.

Fig. 9 shows that mechanical properties of separators fabricated by PIPS was also a function of porosity. Lower porosity resulted in greater elastic moduli (Table 1) and overall strength. This result can be explained by the increasing polymer fraction of less porous samples resulting in a greater effective cross-section, and less internal shear stress. Celgard 2500 has anisotropic mechanical properties where the elastic modulus is much higher in the MD than the transverse direction (TD), a result of the pore-formation step during manufacturing. The stress–strain curves of Celgard 2500 in both the MD and TD (Fig. 9) are consistent with the literature.[75] When applied to LIB cells in a roll-to-roll process, Celgard 2500 is strained in this MD

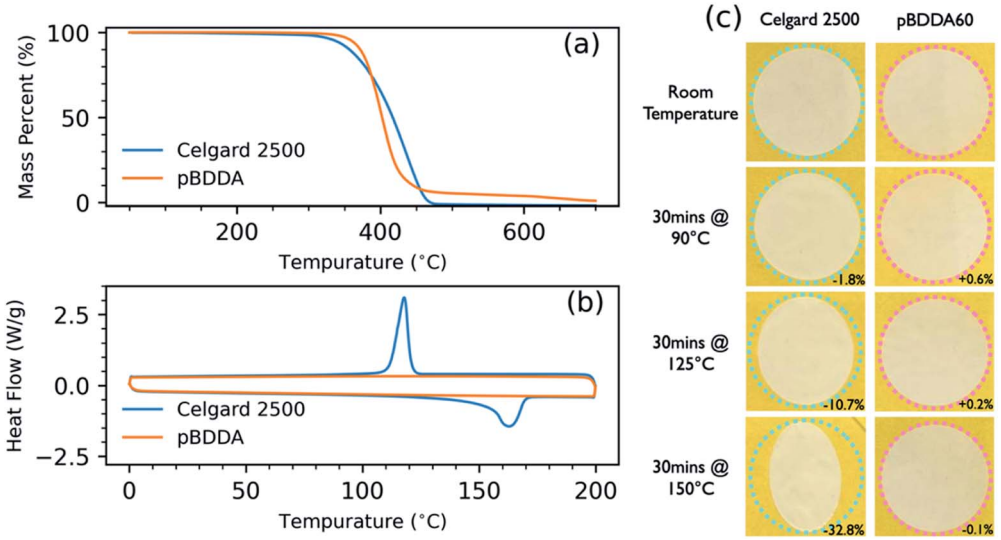

Fig. 8 Thermal characterization of pBDDA and Celgard 2500. (a) Thermogravimetric analysis from 50 °C to 700 °C at a ramp rate of 5 °C min^{-1}. (b) Differential scanning calorimetry from 0 °C to 200 °C at a rate of 10 °C min^{-1}, under nitrogen gas purge. (c) Digital images of Celgard 2500 (25 μm) and pBDDA60 (19 μm) at room temperature and after heating for 30 minutes to 90 °C, 125 °C and 150 °C. The percentages in the bottom right of the images represent the change in separator area.

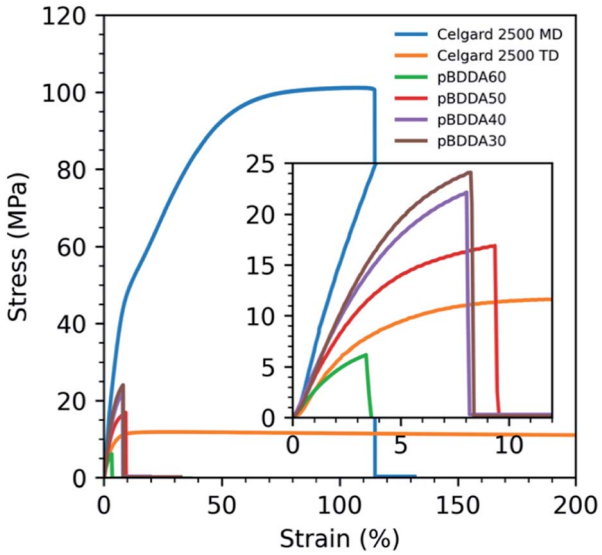

Fig. 9 Stress–strain curves for pBDDA formulations and Celgard 2500 in the machine and transverse directions (MD and TD, respectively). Strain sweep was performed at a constant strain rate of 1% per second.

direction. Due to the method of fabrication outlined, pBDDA samples have isotropic mechanical properties. The modulus of pBDDA60 was 246 MPa which is approximately equal to that of Celgard 2500 in the TD.

Prior studies have found that porous monoliths fabricated by PIPS yield low mechanical strength, but good elastic moduli.[41,42] In LIB applications, the mechanical properties of separators play a relatively small role. Traditionally, the need for sufficient mechanical properties is derived from the manufacturing process of LIBs. Models have been developed to understand the stresses experienced by LIB separators during cycling and have found that these stresses are significantly lower than what is experienced during manufacturing. Thus, forces are well within what membranes fabricated by PIPS can withstand.[76]

The excellent thermal stabilities and mechanical properties of the pBDDA separators stems from the utilization of multifunctional monomers. Photopolymerization of BDDA, which is a di-functional monomer, results in a high degree of polymer chain crosslinking. This crosslinking yields a highly desirable morphology by arresting phase separation during the early stages of spinodal decomposition, producing phase domain sizes on the order of just tens of nanometers. The crosslinking also effectively precludes phase transformations (melting) and increases polymer stiffness, suppressing chain mobility. Other multifunctional acrylate monomers – not limited to difunctional monomers and BDDA – can also be used to generate separators by PIPS; the key is balancing the diffusion of the monomer/porogen system with the kinetics of polymerization (crosslinking) to achieve the ideal polymer morphology.[77,78]

Another variable that can used to tune the separator properties is the choice of porogen. A key requirement is that the porogen remains inert during photopolymerization of the monomer(s). The physicochemical properties of the porogen will also influence the thermodynamics of phase separation *via* the interaction parameter between the monomer/polymer and porogen and the kinetics of spinodal decomposition, controlled primarily through the porogen diffusivity. These cooperative processes determine the domain size of the phase separation. Additional candidates for porogens include other common LIB electrolyte ingredients, such as propylene carbonate (PC), dimethyl carbonate (DMC), vinylene carbonate (VC), fluoroethylene carbonate (FC) and mixed solvent/salt systems.

Conclusions

In this work, we have demonstrated a simple, readily implemented process to manufacture microporous separators using rapid, UV-initiated PIPS. By tuning the precursor concentrations of the reactive multifunctional monomer to porogen (EC in this example), microporous separators with favorable properties (electrolyte uptake, ionic conductivities, thermal stability, *etc.*) are generated in a single processing step. The separators were incorporated into LIB half-cells (NMC532 *vs.* Li) and were shown to cycle reversibly over more than 100 cycles with 98.4% capacity retention with superior rate performance compared to commercial polypropylene separators. A cell was also successfully constructed and cycled without removal of the EC porogen, highlighting the potential for PIPS to be scaled as a fast, inexpensive, one-step LIB manufacturing process. The highly crosslinked polyacrylate chemistry was shown to undergo no phase transitions and was thermally and mechanically stable. Finally, PIPS promises to serve as a platform technology with which separator chemistry and properties can be easy tuned and modified to address current and future challenges in lithium ion batteries.

Conflicts of interest

There are no conflicts to declare.

Acknowledgements

This material is based upon work supported by the National Science Foundation under Grant No. 1845805. This work was supported by the University of Rochester Materials Science Program. The NMC532 electrodes were produced at the U.S. Department of Energy's (DOE) CAMP (Cell Analysis, Modeling and Prototyping) Facility, Argonne National Laboratory. The CAMP Facility is fully supported by the DOE Vehicle Technologies Office (VTO). The authors thank Dr Mark Mathias and Dr Zhuo Li for discussion and advice.

References

1 M. S. Ziegler, J. M. Mueller, G. D. Pereira, J. Song, M. Ferrara, Y.-M. Chiang and J. E. Trancik, *Joule*, 2019, **3**, 2134–2153.
2 R. Schmuch, R. Wagner, G. Hörpel, T. Placke and M. Winter, *Nat. Energy*, 2018, **3**, 267–278.
3 Z. P. Cano, D. Banham, S. Ye, A. Hintennach, J. Lu, M. Fowler and Z. Chen, *Nat. Energy*, 2018, **3**, 279–289.
4 M. Winter, B. Barnett and K. Xu, *Chem. Rev.*, 2018, **118**, 11433–11456.
5 M. F. Lagadec, R. Zahn and V. Wood, *Nat. Energy*, 2019, **4**, 16–25.
6 V. Deimede and C. Elmasides, *Energy Technol.*, 2015, **3**, 453–468.
7 P. Arora and Z. Zhang, *Chem. Rev.*, 2004, **104**, 4419–4462.
8 A. Kwade, W. Haselrieder, R. Leithoff, A. Modlinger, F. Dietrich and K. Droeder, *Nat. Energy*, 2018, **3**, 290–300.
9 W. Zhang, Z. Tu, J. Qian, S. Choudhury, L. A. Archer and Y. Lu, *Small*, 2018, **14**, 1703001.
10 F. A. Susai, H. Sclar, Y. Shilina, T. Rao Penki, R. Raman, S. Maddukuri, S. Maiti, I. C. Halalay, S. Luski, B. Markovsky and D. Aurbach, *J. Adv. Mater.*, 2018, **30**, 1801348.
11 A. Banerjee, B. Ziv, Y. Shilina, J. M. Ziegelbauer, H. Liu, K. J. Harris, G. Botton, G. R. Goward, S. Luski, D. Aurbach and I. C. Halalay, *J. Electrochem. Soc.*, 2019, **166**, A5369–A5377.
12 W. Luo, S. Cheng, M. Wu, X. Zhang, D. Yang and X. Rui, *J. Power Sources*, 2021, **509**, 230372.
13 E. P. Roth, D. H. Doughty and D. L. Pile, *J. Power Sources*, 2007, **174**, 579–583.
14 C. J. Orendorff, T. N. Lambert, C. A. Chavez, M. Bencomo and K. R. Fenton, *Adv. Energy Mater.*, 2013, **3**, 314–320.
15 K. Liu, Y. Liu, D. Lin, A. Pei and Y. Cui, *Sci. Adv.*, 2018, **4**(6), DOI: **10.1126/sciadv.aas9820**.
16 H. Lee, M. Yanilmaz, O. Toprakci, K. Fu and X. Zhang, *Energy Environ. Sci.*, 2014, **7**, 3857–3886.
17 C. M. Costa, Y.-H. Lee, J.-H. Kim, S.-Y. Lee and S. Lanceros-Méndez, *Energy Storage Mater.*, 2019, **22**, 346–375.
18 H. Liao, H. Hong, H. Zhang and Z. Li, *J. Membr. Sci.*, 2016, **498**, 147–157.
19 H. Liang, L. Wan and Z. Xu, *Chinese J. Polym. Sci.*, 2016, **34**, 1423–1435.
20 R. E. Sousa, M. Kundu, A. Gören, M. M. Silva, L. Liu, C. M. Costa and S. Lanceros-Mendez, *RSC Adv.*, 2015, **5**, 90428–90436.
21 A. Banerjee, B. Ziv, Y. Shilina, S. Luski, D. Aurbach and I. C. Halalay, *J. Electrochem. Soc.*, 2016, **163**, A1083–A1094.
22 Z. Li, T. Cao, Y. Zhang, Y. Han, S. Xu and Z. Xu, *J. Membr. Sci.*, 2017, **540**, 422–429.
23 H. Zhang, C.-E. Lin, M.-Y. Zhou, A. E. John and B.-K. Zhu, *Electrochim. Acta*, 2016, **187**, 125–133.
24 D. Li, D. Shi, K. Feng, X. Li and H. Zhang, *J. Membr. Sci.*, 2017, **530**, 125–131.
25 H. Zhang, Y. Zhang, T. Xu, A. E. John, Y. Li, W. Li and B. Zhu, *J. Power Sources*, 2016, **329**, 8–16.
26 D. Li, H. Zhang and X. Li, *J. Membr. Sci.*, 2018, **565**, 42–49.
27 J. Li, W. Tian, H. Yan, L. He and X. Tuo, *J. Appl. Polym. Sci.*, 2016, **133**(30), DOI: **10.1002/APP.43623**.
28 W. Xiao, K. Zhang, J. Liu and C. Yan, *J. Mater. Sci. Mater. Electron.*, 2017, **28**, 17516–17525.
29 D. Li, D. Shi, Y. Xia, L. Qiao, X. Li and H. Zhang, *ACS Appl. Mater. Interfaces*, 2017, **9**, 8742–8750.
30 S. Luiso, A. H. Williams, M. J. Petrecca, S. Roh, O. D. Velev and P. S. Fedkiw, *J. Electrochem. Soc.*, 2021, **168**, 020517.
31 Z. Tabani, H. Maghsoudi and A. Fathollahi Zonouz, *J. Solid State Electrochem.*, 2021, **25**, 651–657.
32 N. Liang, J. Fang and X. Guo, *J. Mater. Chem. A*, 2017, **5**, 15087–15095.
33 D. Lin, D. Zhuo, Y. Liu and Y. Cui, *J. Am. Chem. Soc.*, 2016, **138**, 11044–11050.
34 L. Ye, X. Shi, Z. Zhang, J. Liu, X. Jian, M. Waqas and W. He, *Adv. Mater. Interfaces*, 2017, **4**(11), 1601236.

35 Y. Maeyoshi, S. Miyamoto, H. Munakata and K. Kanamura, *J. Power Sources*, 2017, **350**, 103–108.
36 A. Le Mong and D. Kim, *J. Power Sources*, 2016, **304**, 301–310.
37 H. M. J. Boots, J. G. Kloosterboer, C. Serbutoviez and F. J. Touwslager, *Macromolecules*, 1996, **29**, 7683–7689.
38 N. Tsujioka, N. Ishizuka, N. Tanaka, T. Kubo and K. Hosoya, *J. Polym. Sci., Part A: Polym. Chem.*, 2008, **46**, 3272–3281.
39 O. Okay, *Prog. Polym. Sci.*, 2000, **25**, 711–779.
40 K. Nakanishi and N. Tanaka, *Acc. Chem. Res.*, 2007, **40**, 863–873.
41 E. B. Gienger, P. T. Nguyen, W. Chin, K. D. Behler, J. F. Snyder and E. D. Wetzel, *J. Appl. Polym. Sci.*, 2015, **132**, 42681.
42 K. Sakakibara, H. Kagata, N. Ishizuka, T. Sato and Y. Tsujii, *J. Mater. Chem. A*, 2017, **5**, 6866–6873.
43 M. W. Schulze, L. D. McIntosh, M. A. Hillmyer and T. P. Lodge, *Nano Lett.*, 2014, **14**, 122–126.
44 L. D. McIntosh, M. W. Schulze, M. T. Irwin, M. A. Hillmyer and T. P. Lodge, *Macromolecules*, 2015, **48**, 1418–1428.
45 F. Huang, G. Singer, Y. Zhou, Z. Sha, J. Chen, Z. Han, S. A. Brown, J. Zhang and C. H. Wang, *Compos. Sci. Technol.*, 2021, **207**, 108710.
46 N. Ihrner, W. Johannisson, F. Sieland, D. Zenkert and M. Johansson, *J. Mater. Chem. A*, 2017, **5**, 25652–25659.
47 L. M. Schneider, N. Ihrner, D. Zenkert and M. Johansson, *ACS Appl. Energy Mater.*, 2019, **2**, 4362–4369.
48 OpenCV, Open Source Computer Vision Library, 2015.
49 B. R. Long, S. G. Rinaldo, K. G. Gallagher, D. W. Dees, S. E. Trask, B. J. Polzin, A. N. Jansen, D. P. Abraham, I. Bloom, J. Bareño and J. R. Croy, *J. Electrochem. Soc.*, 2016, **163**, A2999–A3009.
50 A. Udagawa, F. Sakurai and T. Takahashi, *J. Appl. Polym. Sci.*, 1991, **42**, 1861–1867.
51 G. Fini and P. Mirone, *J. Chem. Soc., Faraday Trans. 2*, 1974, **70**, 1776–1782.
52 Z. Wang, *Solid State Ionics*, 1996, **85**, 143–148.
53 N. Saqib, C. M. Ganim, A. E. Shelton and J. M. Porter, *J. Electrochem. Soc.*, 2018, **165**, A4051–A4057.
54 Y.-C. Jung, M.-S. Park, D.-H. Kim, M. Ue, A. Eftekhari and D.-W. Kim, *Sci. Rep.*, 2017, **7**, 17482.
55 K. M. Abraham, *Electrochim. Acta*, 1993, **38**, 1233–1248.
56 H. Lee, Y. Meltem, O. Toprakci, K. Fu and X. Zhang, *Energy Environ. Sci.*, 2014, **7**, 3857–3886.
57 A. Jana, D. R. Ely and R. E. García, *J. Power Sources*, 2015, **275**, 912–921.
58 C. Ishino and K. Okumura, *Eur. Phys. J. E*, 2008, **25**, 415–424.
59 Y. B. Kim, T. Tran-Phu, M. Kim, D.-W. Jung, G.-R. Yi and J. H. Park, *ACS Appl. Mater. Interfaces*, 2015, **7**, 4511–4517.
60 R. Xu, L. Sheng, H. Gong, Y. Kong, Y. Yang, M. Li, Y. Bai, S. Song, G. Liu, T. Wang, X. Huang and J. He, *Adv. Energy Mater.*, 2021, **23**(3), DOI: **10.1002/adem.202001009**.
61 H. Zhang, M.-Y. Zhou, C.-E. Lin and B.-K. Zhu, *RSC Adv.*, 2015, **5**, 89848–89860.
62 K. K. Patel, J. M. Paulsen and J. Desilvestro, *J. Power Sources*, 2003, **122**, 144–152.
63 J. Landesfeind, J. Hattendorff, A. Ehrl, W. A. Wall and H. A. Gasteiger, *J. Electrochem. Soc.*, 2016, **163**, A1373–A1387.
64 D. Djian, F. Alloin, S. Martinet, H. Lignier and J. Y. Sanchez, *J. Power Sources*, 2007, **172**, 416–421.
65 W. D. Callister and D. G. Rethwisch, *Materials Science and Engineering: An Introduction*, John Wiley and Sons, 2013.
66 S. J. Kwon, S.-E. Lee, J.-H. Lim, J. Choi and J. Kim, *Electronics*, 2018, **7**(12), DOI: **10.3390/electronics7120406**.
67 W. Xu, J. Wang, F. Ding, X. Chen, E. Nasybulin, Y. Zhang and J.-G. Zhang, *Energy Environ. Sci.*, 2014, **7**, 513–537.
68 J. Xiao, Q. Li, Y. Bi, M. Cai, B. Dunn, T. Glossmann, J. Liu, T. Osaka, R. Sugiura, B. Wu, J. Yang, J.-G. Zhang and M. S. Whittingham, *Nat. Energy*, 2020, **5**, 561–568.
69 I. C. McNeill and M. H. Mohammed, *Polym. Degrad. Stab.*, 1995, **48**, 175–187.
70 G. G. Botte, R. E. White and Z. Zhang, *J. Power Sources*, 2001, **97–98**, 570–575.
71 B. Ravdel, K. M. Abraham, R. Gitzendanner, J. DiCarlo, B. Lucht and C. Campion, *J. Power Sources*, 2003, **119–121**, 805–810.
72 R. E. Gerver and J. P. Meyers, *J. Electrochem. Soc.*, 2011, **158**(7), A835–A843.
73 G.-H. Kim, K. Smith, K.-J. Lee, S. Santhanagopalan and A. Pesaran, *J. Electrochem. Soc.*, 2011, **158**(8), A955–A969.
74 Y. Li, L. Yu, W. Hu and X. Hu, *J. Mater. Chem. A*, 2020, **8**, 20294–20317.
75 X. Zhou, L. Yue, J. Zhang, Q. Kong, Z. Liu, J. Yao and G. Cui, *J. Electrochem. Soc.*, 2013, **160**, A1341–A1347.
76 D. Shi, X. Xiao, X. Huang and H. Kia, *J. Power Sources*, 2011, **196**, 8129–8139.
77 N. Boyard, M. Vayer, C. Sinturel, S. Seifert and R. Erre, *Eur. Polym. J.*, 2005, **41**, 1333–1341.
78 N. Boyard, M. Vayer, Ch. Sinturel and R. Erre, *J. Appl. Polym. Sci.*, 2005, **95**, 1459–1472.